

THE CREEP BEHAVIOR OF LONG FIBER REINFORCED THERMOPLASTICS

EXAMINED BY MICROSTRUCTURAL SIMULATIONS

S. Fliegner^a, J. Hohe^a, P. Gumbsch^{a, b}

Corresponding author: S. Fliegner, sascha.fliegner@iwm.fraunhofer.de

a) Fraunhofer Institute for Mechanics of Materials IWM, Freiburg, Germany

b) Institute for Applied Materials, Karlsruhe Institute of Technology, Karlsruhe, Germany

Abstract: Long fiber reinforced thermoplastics (LFT) appear to be promising for the cost efficient manufacture of lightweight structures by injection or compression molding. One major concern persists in their inherent tendency to creep due to continuous sliding within the thermoplastic matrix. To enable the application of LFT components under significant static loads, a profound knowledge of the interactions between the viscoelastic matrix and the nonwoven, discontinuous fiber reinforcement is necessary. In the present work, these interactions are investigated by micromechanical finite element simulations of computer generated LFT structures. The viscoelastic properties of the neat matrix are experimentally characterized and implemented into the microstructural models by an appropriate constitutive law in the form of a four parameter Burgers model. Since a distinct degree of nonlinearity is observed, the applied model is extended to the nonlinear viscoelastic regime and found to be suitable for an accurate reproduction of the experimental data. Micromechanical creep simulations which incorporate the viscoelastic matrix behavior are then validated against creep experiments on LFT specimens of three material variants with a different fiber fraction (PPGF10, PPGF20 and PPGF30), which are loaded under two different orientations at multiple stress levels. The model predictions show a good agreement to the experimental results in particular for the lower and medium stress levels, whereas a slightly increased error can be observed for the highest stress levels. By the application of different variants of the viscoelastic matrix model it is shown that the effects of nonlinearity on the effective creep

behavior of the composite are quite considerable. Finally, the evolution of stress and strain within the microstructure during the creep period is visualized by contour plots at different times. The redistribution of stress from the viscoelastic matrix to the elastic fibers can clearly be observed.

Keywords: Long fiber reinforced thermoplastics (LFTs), A. Polymer-matrix composites (PMCs), B. Creep, C. Finite element analysis (FEA), C. Multiscale modeling

1. Introduction

Thermoplastic matrix composites like long fiber reinforced thermoplastics (LFT) gain increasing importance for the manufacturing of lightweight structures in automotive industry. They represent a good tradeoff between the mechanical performance and costs due to their suitability for mass production by technologies like injection or compression molding and their sufficiently high fiber length, resulting in a high mass related strength [1]. Furthermore, they are recyclable due to the reversibility of the solidification process of the thermoplastic matrix. However, a limitation toward the application in structural parts under significant static loads persists due to their inherent tendency to creep deformation. This results from the load driven, continuous sliding of the polymeric chains of the thermoplastic matrix. The lack of a side-chain network, as compared to thermosets, is responsible for the more pronounced creep. Whereas the viscoelastic properties of monolithic thermoplastic materials were studied to a rather high degree, only few works have been reported on fiber reinforced thermoplastics. This applies in particular to discontinuous fiber reinforced composites with a nonwoven structure. To enable their application in structural parts, a profound understanding of the microstructural interactions between the thermoplastic matrix and the fibers is of crucial importance.

A variety of viscoelastic models has been proposed in the literature. Most of them were originally developed to describe the mechanical behavior of bulk polymeric materials, but can also be applied to composites or - within a microstructural model - to describe the viscoelastic phase of the composite. These include the classical Maxwell and Kelvin-Voigt elements and their combination to the four parameter Burgers model. Usually, Boltzmann's superposition principle in the form of convolution integrals is applied for their mathematical description, yielding the memory function, restricted to linear viscoelastic behavior in its original form. Fundamental contributions toward the extension to nonlinear viscoelasticity by the introduction of nonlinearizing functions into the convolution integral were made by Leaderman [2]. Schapery [3] proposed a more general and thermodynamically consistent form of Leaderman's modified superposition principle, which is widely accepted today. Findley *et al.* [4] followed a different route by describing the time-dependent deformation by a power law, which is restricted to a single relaxation time in contrast to the Schapery model. A variety of finite element implementations of such models and their application to various loading scenarios is presented in the literature. Lai and Bakker [5] and Haj-Ali and Muliana [6] described the implementation of the Schapery model. An excellent overview and comparison of multiple models with respect to their numerical implementation was given by Woldekidan [7].

A general review of the creep behavior of polymer matrix composites (PMCs) and related experimental and modeling techniques to characterize them was published by Scott *et al.* [8]. Macroscopic material laws applicable to fiber reinforced plastics were presented by Lou and Schapery [9]. Greco *et al.* [10] studied the flexural creep of a thermoplastic composite with a woven structure and applied an analytical model to describe the experimental findings. The influence of a varying fiber volume fraction on the creep behavior of polypropylene-based composites has been examined by Houshyar *et al.* [11]. Howard and Hollaway [12] characterized a randomly oriented glass fiber / polyester composite and applied the Schapery

model to describe the experimental data. All these approaches are restricted to the macroscopic level - the micromechanical interactions within the heterogeneous materials are not considered.

Micromechanical methods which determine the effective composite properties based on the constituent behavior are widely used to predict the elastic properties. In contrast, relatively few works extend the classical homogenization schemes to viscoelasticity. Such methods usually include a viscoelastic description of the matrix, the fibers or the interface to represent their time-dependent behavior. Analytical approaches like the Mori-Tanaka scheme [13] offer the advantage of very low computing times but require significant simplifications with respect to the geometry and the interactions of the inclusions. The analytical approaches were found to be sufficiently accurate to describe the time-independent, elastic properties of LFTs with a distinct fiber orientation and length distribution [14,15,16]. However, this is not necessarily the case for their viscoelastic behavior. Finite element (FE) models which explicitly depict the microstructure in the form of representative volume elements (RVEs) overcome these simplifications, but they usually require massive computational resources. Brinson and Lin [17] used the Mori-Tanaka approach to model a composite of viscoelastic phases by the application of the elastic-viscoelastic correspondence principle and compared it to FE simulations of a unidirectional composite. Brinson and Knauss [18] analyzed multiphase, viscoelastic solids by FE simulations. Matzenmiller and Gerlach [19] presented a micromechanical model of viscoelastic composites with compliant fiber-matrix bonding based on the generalized method of cells. Viscoelastic interphases were also treated by Fisher and Brinson [20]. The nonlinear viscoelastic behavior of laminated composites was examined by Haj-Ali and Muliana [21] by combining the Schapery model to describe the matrix and a four-cell micromodel to account for the unidirectional, elastic fibers.

Specific micromechanical models to describe the creep behavior of a nonwoven fiber structure with a distinct fiber orientation and length distribution are currently not available.

Therefore, this work extends a microstructural model for LFTs [22,23] to include a viscoelastic description of the matrix to examine its creep behavior. For this purpose, artificial LFT structures of three materials with different fiber fractions are generated under compliance of experimentally measured microstructural data: fiber orientation distribution, fiber length distribution and fiber volume fraction (Section 3.1). The viscoelastic properties of the matrix are determined on substance specimens of the neat matrix. Based on the experimental findings, an appropriate constitutive law in the form of a four parameter Burgers model is implemented into the FE software and calibrated on the creep tests (Section 3.2). Since the experimental results reveal a strong degree of nonlinearity, the model is extended to the nonlinear viscoelastic regime. Finally, creep simulations are performed on the computer generated LFT microstructures using the viscoelastic matrix model. The predictions are compared to experimental creep tests on LFT specimens in Section 4.1. To visualize the effects of the nonlinear matrix behavior on the effective creep curves of the composite, different variants of the viscoelastic constitutive law are applied and compared. Moreover, the evolution of microscopic stress and strain is studied by contour plots of the microstructure at different times (Section 4.2). Potential applications of our model are discussed in Section 4.3.

2. LFT material and experimental methods

The investigated LFT material consists of a polypropylene matrix (*DOW® C711-70RNA*) and glass fibers (*TufRov® 4575*). Three material variants PPGF10, PPGF20 and PPGF30 were produced with different fiber weight fractions of 10, 20 and 30 wt-% (corresponding fiber volume fractions of 3.8, 8.2 and 13.2 vol-%). PPGF30 and PPGF20 are of special interest for structural application and commonly used by the automotive industry, whereas PPGF10 is rather of academic interest to provide additional data for the model validation. Plates with dimensions of 400 x 400 x 3 mm³ were manufactured by compression molding as described by Henning *et al.* [24]. The LFT strand as it came out of the extruder was positioned

asymmetrically in the mold. The material flow during the compression of the mold generates a rather high degree of fiber orientation everywhere outside the strand inlay position. This so-called flow region of the plate was investigated in the following. For mechanical testing, tensile specimens were machined in 0° (flow direction) and 90° (transverse direction) relative to the mean orientation of the fibers. Micro computer tomographic (CT) measurements were conducted to determine the fiber orientation distribution of the material which is required for the microstructural models. The fiber length distribution was determined by analysis of incinerated specimens. More details of these procedures are given in previous contributions [22,23]. To measure the mechanical properties of the neat polypropylene, matrix substance specimens were manufactured by injection compression molding. To ensure the mechanical compatibility between the matrix specimens and the matrix within the LFT samples, the same coupling agents and stabilizers as used in the LFT process were added for the matrix substance specimens.

Creep tests on matrix and LFT specimens (geometry according to DIN EN ISO 3167 with a reduced section of $70 \times 10 \times 3 \text{ mm}^3$) were performed at standard climate (23°C temperature, 50 % relative humidity). At the beginning of the load period of $6 \cdot 10^5 \text{ s}$, a load defined by the product of specimen cross section and desired nominal stress level was applied in the form of a lead weight. For the lower stress levels up to 5 MPa, the load was directly attached to the specimen clamps, whereas a lever mechanism with a transmission ratio of 10 was used for the higher stress levels. The strain was measured with an *Instron*[®] 2620-604 axial clip-on extensometer with a gauge length of 50 mm. Up to a time of 3600 s, a recording interval of 1 s was chosen for data acquisition. Thereafter - up to the total testing time of $6 \cdot 10^5 \text{ s}$ - the recording interval was increased to 600 s.

3. Modeling

3.1. Computer generation of LFT structures

The applied structure generation procedure suitable for the reproduction of the complex nonwoven fiber structure of the LFT material is described in [22,23]. An alternative voxel discretization of the same structures is presented in [25]. A stack of straight fibers with dilute concentration is generated according to the desired planar fiber orientation and length distribution. The fibers are then compressed in a FE simulation until a realistic value of fiber volume fraction is reached. A contact formulation prevents interpenetration of adjacent fibers and fiber waviness develops in analogy to the manufacturing process of the real material produced by compression molding. Finally, the deformed fibers are placed in a cuboid volume and the remaining gaps are filled with a tetrahedral mesh representing the matrix.

A close-up of the mesh for an exemplary structure is shown in Fig. 1. A small section of a computer generated fiber structure is compared to a section of the corresponding CT scan in Fig. 2 (left). A high degree of similarity can be observed with respect to characteristic features like fiber waviness and packing density. However, the depicted sections are too small to fully represent the measured fiber orientation. Therefore, the fiber orientation distributions (probability density functions of the in-plane fiber angles) of the computer generated structure and the corresponding CT scan are compared in Fig. 2 (right) for the complete analyzed volume. For this purpose, the same image correlation technique based on the plugin *Directionality for ImageJ* [26] was applied on two dimensional images of the artificial structure and the CT scan. The images were extracted by equidistant cuts through the LFT structure and the CT scan. The computer generated structures agree well with experimental data and are therefore well suited for the micromechanical simulations. This said, it is noted that the applied procedure represents a pragmatic way to generate a nonwoven fiber structure and does not account for the complex physical mechanisms which govern the evolution of the microstructure during the compression molding process in reality. Furthermore, it is worth mentioning that even if the computer generated structures are based on statistical distributions in the form of a fiber orientation and length distribution, they cannot be referred to as a

classical representative volume element (RVE) since the separation of scales is not possible for the present material: The maximum fiber length (50 mm) is not small compared to the maximum dimensions of the volume element (50 mm) or (in some cases) of the whole part. Further discussion and a study of the influence of varying dimensions of the structures can be found in [23].

In this work, the creep behavior of the same structures which were previously investigated with respect to their elastic properties [22] is studied. These include the computer generated microstructures for LFT materials with three different fiber fractions (PPGF10, PPGF20 and PPGF30, see Table 1). Time-independent, elastic fiber properties (see Table 2) and a perfect interface were assumed and viscoelastic behavior of the polypropylene matrix was implemented into the simulations as described next.

3.2. Viscoelastic matrix model

3.2.1 Model choice

Motivated by the experimental findings (Section 3.2.3), the Burgers model is considered as the most realistic mathematical description of the viscoelastic behavior of the polypropylene matrix. Due to its feature of a free dashpot (η_0 , Fig. 3), the viscous character of the model is dominant and thus a stationary creep rate results after the relaxation of the Kelvin-Voigt element (E_1 and η_1). This corresponds to the assumption of a continuous sliding of the polymeric chains under load. It is coupled to an irreversible strain component which remains during the recovery phase after unloading. These common characteristics of amorphous or semi-crystalline thermoplastics could also be observed for the investigated polypropylene and motivate the choice of the model. The experimental results described later also reveal a strong nonlinearity of the creep curves as a function of stress. It is therefore mandatory to extend the Burgers model to the nonlinear viscoelastic regime. An alternative would have been to fit the Schapery model [3] to the experimental data. Since the Schapery model is based on a

generalized Maxwell model which does not feature a free dashpot, it is more appropriate to model the response of thermosetting materials, as discussed by Brinson [27]. Therefore, the Schapery model is less adequate for the thermoplastic polypropylene matrix treated in this work.

3.2.2 Model formulation and implementation

A general form of the one dimensional constitutive equation of the Burgers model can be derived in the form of the differential equation

$$\frac{E_1}{\eta_0} \sigma + \left(1 + \frac{E_1}{E_0} + \frac{\eta_1}{\eta_0}\right) \dot{\sigma} + \frac{\eta_1}{E_0} \ddot{\sigma} = E_1 \dot{\varepsilon} + \eta_1 \ddot{\varepsilon} \quad (1)$$

with the elastic stiffness of the springs E_0, E_1 and the viscosity of the dashpots η_0, η_1 (Fig. 3).

Eq. 1 can be solved under the boundary condition of a constant stress σ_0 (corresponding to the load case of creep). The time-dependent part, denoted as creep compliance $C(t)$, can then be separated:

$$\varepsilon(t) = \sigma_0 \left[\frac{1}{E_0} + \frac{t}{\eta_0} + \frac{1}{E_1} \left(1 - e^{-\frac{t}{\tau}}\right) \right] = \sigma_0 C(t) \quad (2)$$

where $\tau = \eta_1 / E_1$ denotes the relaxation time of the Kelvin-Voigt element.

To describe more general loading scenarios, the creep compliance $C(t)$ can be combined with an arbitrary load history by Boltzmann's superposition principle (also known as memory function), resulting in the convolution integral with the time integration variable τ :

$$\varepsilon(t) = \int_0^t C(t - \tau) \dot{\sigma} \, d\tau \quad (3)$$

In its original form, the superposition principle suffers from the major restriction to linear viscoelasticity (the creep response being independent of load).

For numerical implementation into a finite element framework, the memory function (Eq. 3) is converted to an incremental form. It is then no longer necessary to integrate the strain response over the complete load history, since a recursive form can be derived in analogy to

the work of Taylor *et al.* [28], where the strain of the Kelvin-Voigt element is inherited from the previous to the current time increment. The incremental approach is also advantageous for the extension of the model to the nonlinear viscoelastic regime, since the global nonlinear behavior can be approximated by a series of sectional linear time increments. To derive the incremental form of the Burgers model, the total strain increment $\Delta\varepsilon^{\text{tot}}$ is decomposed into an elastic $\Delta\varepsilon^e$, a viscous $\Delta\varepsilon^v$ and a viscoelastic $\Delta\varepsilon^{\text{ve}}$ part as follows:

$$\Delta\varepsilon^{\text{tot}} = \Delta\varepsilon^e + \Delta\varepsilon^v + \Delta\varepsilon^{\text{ve}} = \Delta\sigma C(t) = \Delta\sigma[C^e(t) + C^v(t) + C^{\text{ve}}(t)] \quad (4)$$

Each component $\varepsilon(t)$ is then transformed to its incremental form $\Delta\varepsilon(t)$. The detailed derivation can be found in the work of Woldekidan [7] and is omitted here. The strain components in incremental form are given by:

$$\Delta\varepsilon^e = \frac{\Delta\sigma}{E_0} \quad (5)$$

$$\Delta\varepsilon^v = \frac{\Delta t}{\eta_0} \left[\sigma(t - \Delta t) + \frac{\Delta\sigma}{2} \right] \quad (6)$$

$$\Delta\varepsilon^{\text{ve}} = \frac{\Delta\sigma}{E_1} - \left[e^{-\frac{\Delta t}{\tau}} - 1 \right] \varepsilon^{\text{inh}}(t - \Delta t) - \frac{1}{E_1} \frac{\Delta\sigma}{\Delta t} \tau \left[1 - e^{-\frac{\Delta t}{\tau}} \right] \quad (7)$$

where $\varepsilon^{\text{inh}}(t - \Delta t)$ denotes the inherited strain of the Kelvin-Voigt element from the previous time increment and $\tau = \eta_1 / E_1$ the relaxation time.

In the following, the incremental form of the linear viscoelastic Burgers model (Eq. 4 - 7) is generalized to three dimensions under the assumption of isotropic behavior of the neat polypropylene matrix within the composite. Therefore, the one dimensional creep compliance $C(t)$ is decomposed into a shear J and a bulk component B with a time-independent, constant Poisson's ratio ν :

$$J(t) = 2(1 + \nu)C(t) \quad (8)$$

$$B(t) = 3(1 - 2\nu)C(t) \quad (9)$$

$$\nu = \text{const.} \quad (10)$$

These assumptions affect the viscoelastic response to be compressible in analogy to an elastic solid and thus both the shear and the bulk components of the viscoelastic deformation to be time-dependent. According to Lai and Bakker [5], such treatment is justified for semi-crystalline thermoplastics as the investigated polypropylene.

The three dimensional, linear viscoelastic Burgers model in incremental form can be expressed by the combination of Eq. 8 - 10 with Eq. 4 - 7. For this purpose, the strain tensor is decomposed into deviatoric and volumetric components, for which the time-dependent response can then be calculated separately under application of $J(t)$ and $B(t)$, respectively (Eq. 8 - 9). More details and the fully three dimensional equations can be found in the appendix and the work of Woldekidan [7]. Due to its recursive formulation, a very efficient numerical implementation is enabled and the calculation of the current stress increment $\Delta\sigma$ is possible with the knowledge of the current strain increment $\Delta\varepsilon(t)$ and the inherited strain $\varepsilon^{\text{inh}}(t-\Delta t)$ from the previous time increment, stored in history variables at each integration point.

Motivated by the experimental findings on matrix substance specimens (Section 3.2.3), where a nonlinear viscoelastic response and thus, a distinct stress-dependence of the Burgers parameters is observed, the model has to be extended to the nonlinear viscoelastic regime.

This is done in analogy to the modified superposition principle, introduced by Leaderman [2].

The nonlinear viscoelastic behavior is treated numerically by the consideration of stress-dependent model parameters E_1 , η_0 and η_1 , which are implicitly calculated for each time increment Δt . The material subroutine needs therefore to be extended by a Newton-Raphson procedure to identify the model parameters as shown in Fig. 4: First, a trial stress increment $\Delta\sigma_{\text{tr}}$ is calculated based on the model parameters of the previous time increment. The stress-dependent model parameters are then updated with this trial stress σ_{tr} (as detailed in Section 3.2.3). Using the updated model parameters, the trial stress increment $\Delta\sigma_{\text{tr}}$ is transformed to a trial strain increment $\Delta\varepsilon_{\text{tr}}$. A residual strain increment $\Delta\varepsilon_{\text{res}} = \Delta\varepsilon_{\text{tr}} - \Delta\varepsilon$ between the trial strain

increment $\Delta\epsilon_{tr}$ and the strain increment $\Delta\epsilon$, provided by the FE software, can then be formed. If the Eulerian norm of $\Delta\epsilon_{res}$ is larger than a specified tolerance, it is minimized by a iterative Newton-Raphson loop by choosing a new trial stress increment $\Delta\sigma_{tr}$ and repeating the procedure until the norm of the residual strain increment $\Delta\epsilon_{res}$ is sufficiently small. In order to provide a scalar equivalent stress to describe the stress-dependence of the model parameters, the von Mises stress σ_{eq} (Eq. 14) is calculated from the trial stress tensor $\sigma_{tr} = \sigma(t-\Delta t) + \Delta\sigma_{tr}$. The stress-dependent model parameters E_1 , η_0 and η_1 are then derived based on the empirical functions specified in Section 3.2.3.

3.2.3 Model calibration

The model parameters as applied for the microstructural simulations presented in Section 4 are summarized in Table 2. To calibrate the model, the creep function (Eq. 2) was fitted to the experimental data of creep-recovery experiments on matrix substance specimens (Fig. 5) for each individual stress level by application of a least squares procedure. In this way, a set of Burgers parameters E_0 , E_1 , η_0 , η_1 was identified for each discrete stress level. It is remarkable that the shape of the experimental curves (Fig. 5) can be reproduced by the model to a very high level of accuracy and that the irreversible strain component of the recovery period is well captured (as discussed in Section 3.2.1). It is evident that the slope of the creep curves increases significantly with stress, which indicates a strong nonlinear viscoelastic behavior. This nonlinearity is accounted for by empirical functions which mimic a stress dependence of the model parameters. Three of the four Burgers parameters (E_1 , η_0 , η_1) show a distinct stress dependence, whereas the instantaneous elastic stiffness E_0 was found to be independent of stress and assigned to a constant value of $E_0 = 1250$ MPa. To visualize this dependency, the values of E_1 , η_0 , η_1 as determined by the creep-recovery experiments are plotted against the stress in Fig. 6 (symbols). The stress dependence can be described by empirical functions (Eq.

11-13) which are shown as lines in the same figure. These equations were used to calculate the stress-dependent model parameters in the material subroutine (Section 3.2.2, Fig. 4):

$$E_1 = 3292.34 \text{ MPa} \cdot 0.86788 \sigma_{\text{eq}}/\text{MPa} \quad (11)$$

$$\eta_0 = 3.0602 \cdot 10^9 \text{ MPa} \cdot \text{s} - 1.11126 \cdot 10^9 \text{ MPa} \cdot \text{s} \cdot \ln(\sigma_{\text{eq}}/\text{MPa} - 0.4369) \quad (12)$$

$$\eta_1 = 5.38979 \cdot 10^7 \text{ MPa} \cdot \text{s} - 1.78557 \cdot 10^7 \text{ MPa} \cdot \text{s} \cdot \ln(\sigma_{\text{eq}}/\text{MPa} - 1.73967) \quad (13)$$

where the equivalent stress σ_{eq} refers to the unidirectional stress for the creep experiments and the von Mises stress (Eq. 14) for the three dimensional model, respectively.

4. Results and discussion

4.1 Effective behavior / macroscopic creep curves

Three variants of the microstructural model, featuring a different fiber fraction (PPGF10, PPGF20, PPGF30, see Table 1) were analyzed by FE simulations under application of the viscoelastic matrix model. Their unidirectional creep response was compared to corresponding experiments on LFT specimens to validate the modeling approach. A period of $6 \cdot 10^5$ s (approximately one week) was chosen which is identical to the time period of the calibration experiments on matrix substance specimens (Section 3.2.3). Two different orientations with the load direction parallel to the flow direction (0°) and transverse to the flow direction (90°) were studied. The stress levels were chosen in the range up to approximately 50 % of the quasi static strength for each material variant and orientation. The results are shown in Fig. 7 - 9. Overall, a good agreement between the experiments and the simulations is observed. The maximum deviation is mostly within the range of tolerance of the strain measurement device of approximately 0.0005 strain. For the lower and medium stress levels (PPGF10: 3.3 and 10 MPa in 0° , 2.5 MPa in 90° load direction, Fig. 7 / PPGF20: 10 and 20 MPa in 0° , 5 MPa in 90° load direction, Fig. 8 / PPGF30: 15 and 25 MPa in 0° , 5 MPa in 90° load direction, Fig. 9) the deviation between simulations and experiments is

particularly low and also the almost constant creep rate of the simulations in the range of $2 \cdot 10^5$ to $6 \cdot 10^5$ s fits well to the experimental results. For the highest stress levels (PPGF10: 15 MPa in 0° , 5 MPa in 90° load direction, Fig. 7 / PPGF20: 30 MPa in 0° , 7.5 MPa in 90° load direction, Fig. 8 / PPGF30: 40 MPa in 0° , 7.5 MPa in 90° load direction, Fig. 9), the error of the predictions is slightly increased: In particular, the creep rate above $2 \cdot 10^5$ s is overestimated by the simulations. Possibly, a more accurate calibration of the viscoelastic matrix model at higher stresses would be needed to increase the precision, e.g. by evaluation of more experimental data and a finer incrementation of the stress levels (e.g. increments of 0.5 to 1 MPa instead of the current value of 2.5 MPa, see Fig. 5). Another reason could be the presence of plastic deformation within the matrix at higher stress levels, which is not captured by the purely viscoelastic model, even if all investigated stress levels are significantly below the macroscopic yield strength for each material variant. In 90° load direction, the microstructures are not expected to be representative due to the drastically reduced dimensions in transverse direction (PPGF30: 1.5 mm - PPGF20 & PPGF10: 2.75 mm, see Table 1) compared to the flow or longitudinal direction (50 mm for all materials). Thus, the structures do not represent the fiber length distribution (with a maximum fiber length of 50 mm) adequately in this direction (90°) and precision of the models is lost. To address this issue, an additional set of LFT structures which incorporate a much larger fraction of the fiber length distribution in transverse direction would be necessary.

The effects of the nonlinearity of the polypropylene matrix on the effective creep behavior of the composite were studied by comparing simulated creep curves for different variants of the matrix model and an exemplary structure (PPGF30, 0° load direction, 40 MPa stress) in Fig. 10. The nonlinear model (stress dependent parameters, Eq. 11-13) is compared to the linear model (constant parameters) which was fed with the highest and lowest values for E_1 , η_0 and η_1 of the investigated range (Fig. 6, Table 2), yielding a lower and upper boundary curve. It

can be seen that the difference between the boundary curves is quite large and that the nonlinear model clearly shows the best agreement with the experimental data. It is thus concluded that a linear viscoelastic model cannot be applied with reasonable accuracy since the effects of the nonlinear viscoelastic behavior of the matrix are significant.

4.2 Evolution of stress and strain fields at the microscopic level

The evolution of the stresses and strains within the microstructure of an exemplary structure of PPGF30, 0° load direction and the highest investigated stress level of 40 MPa is shown in Fig. 11 for two points of time (600 s and 6·10⁵ s), which represent the beginning of the creep period shortly after the application of the load (600 s) and at an advanced state (6·10⁵ s). To visualize the redistribution of stress and strain within the microstructures, the following equivalent measures are introduced and assigned to the color scale of the contour plots:

$$\sigma_{\text{eq}} = \sqrt{\frac{3}{2} \sigma'_{ij} \sigma'_{ij}} \quad (14)$$

$$\varepsilon'_{\text{eq}} = \frac{1}{1+\nu} \sqrt{\frac{3}{2} \varepsilon'_{ij} \varepsilon'_{ij}} \quad (15)$$

$$\varepsilon_{\text{H}} = \frac{1}{3} \varepsilon_{kk} \quad (16)$$

where σ_{eq} denotes the von Mises equivalent stress, ε'_{eq} the equivalent deviatoric strain (in analogy to the von Mises form) and ε_{H} the hydrostatic strain. σ'_{ij} and ε'_{ij} are the deviatoric stress and strain tensor, respectively.

Fig. 11 (top) shows the stress redistribution within the composite material during creep. With increasing time, creep in the matrix decreases its load carrying capability and therefore, the load is subsequently shifted to the time-independent, elastic fibers. At the beginning of the creep period, the maximum von Mises stress within the fibers amounts to approximately 1150 MPa (maximum value of the color scale). At the end of the creep period of 6·10⁵ s, the maximum value has significantly increased to approximately 2000 MPa, which is still below

the nominal fracture stress of the glass fibers of approximately 2500 MPa. This agrees well to the experimental observations, where no creep fracture could be observed even for the highest investigated stress level of 40 MPa (Fig. 9 left).

In Fig. 11 (middle and bottom), the deviatoric and volumetric strain components of the matrix are visualized by respective measures (Eq. 15 and 16). It is remarkable that the equivalent deviatoric strain (Fig. 11 middle, scale maximum of 0.05) is significantly larger than the equivalent volumetric (hydrostatic) strain (Fig 11 bottom, scale maximum of 0.01) anywhere and to any time within the investigated structure. This indicates that although a volumetric component of time-dependent deformation is accounted for by the viscoelastic matrix model, the dominant deformation mechanism within the microstructures is governed by shear.

4.3 Potential applications of the model

As mentioned in the introduction, models to describe the time-dependent deformation of LFTs are mandatory to enable the application of the material in components under significant static loads. The proposed approach offers the advantage that the time dependent matrix properties can be experimentally characterized on neat substance specimens which feature isotropic behavior. Thus, the number of calibration experiments can be significantly reduced since no dependence on the load direction exists. The influence of the fibers on the effective creep behavior is then computed by the FE model. Instead of experimental data of the microstructure, arbitrary orientation states (e.g. from process simulation at multiple positions within a part) could be fed into the model. However, the proposed model appears not to be suitable for integrative simulation of components in the near future due to the high computation times. Instead, a multiple step procedure seems more realistic, in which our model can provide additional data for the development and the calibration of novel effective creep laws. Within this framework, our model may act as a powerful tool for the virtual development of materials accounting properly for all essential microstructural features. Based

on the homogenization results obtained thereby, appropriate macroscopic constitutive equations to describe the material can be derived and used in structural analyses. In contrast, mean field homogenization schemes based on Eshelby's solution (like the Mori-Tanaka model [13]) cannot describe a variation of stress within the matrix phase. However, our work shows that such variations need to be accurately captured since the matrix material shows a distinct nonlinear viscoelastic behavior and the effects on the creep behavior are quite considerable (see Fig. 10). This is also the case if local damage mechanisms are of interest. In the future, it is therefore necessary to develop new analytical approaches which account for such effects. These models can then be precisely calibrated on microstructural models like ours. Another application could be the use of time-temperature superposition principles: As discussed by Brinson [29], a global thermorheologically complex behavior of the composite can be decomposed into thermorheologically simple phases by the application of a micromechanical FE model. Thus, superposition techniques like the time-temperature correspondence principle can be applied to the constituents. In contrast, no such treatment is justified at the homogenized effective level.

5. Conclusions

A micromechanical finite element model to describe the creep behavior of long fiber reinforced thermoplastic was proposed, accounting for their characteristic, discontinuous nonwoven fiber structure, using a viscoelastic constitutive law to describe the time-dependent behavior of the matrix. It was shown that the creep behavior on the effective composite level can be accurately described based on the knowledge of the constituent properties and the microstructural characteristics. A classical four parameter Burgers model was chosen to describe the creep behavior of the matrix and calibrated with creep experiments on matrix substance specimens. Motivated by the experimental findings which reveal a high degree of nonlinearity within the viscoelastic range, the model was modified to account for these effects

by empirical functions which mimic the stress dependence of the model parameters. The effects of the nonlinearity of the matrix on the creep behavior of the composite were found to be significant. The evolution of stresses and strains within the microstructure was visualized by respective contour plots. The hydrostatic and deviatoric components of strain were quantified by effective measures. It was found that the deviatoric components play the major role in the time-dependent deformation of the matrix, whereas the effects of the hydrostatic components are rather weak.

6. Acknowledgements

This work was partially funded by the German Research Foundation (International Research Training Group GRK 2078). The authors would like to thank B. Hangs (Fraunhofer ICT) for providing the material and A. Fink, M. Kabel (Fraunhofer ITWM) as well as D. Elmer, T. Seifert (Offenburg University of Applied Sciences) for their support and inspiring discussions.

7. Appendix

In the following, the three dimensional, incremental form of the nonlinear Burgers model is specified in analogy to the work of Woldekidan [7]. For this purpose, the Voigt form of the stress and strain tensors is chosen in favor to a compact notation (vectors, tensors and matrices are printed in bold, up to second order in lower case, above in upper case):

$$\boldsymbol{\sigma} = [\sigma_{11} \ \sigma_{22} \ \sigma_{33} \ \sigma_{23} \ \sigma_{13} \ \sigma_{12}] \quad (\text{A.1})$$

$$\boldsymbol{\varepsilon} = [\varepsilon_{11} \ \varepsilon_{22} \ \varepsilon_{33} \ 2\varepsilon_{23} \ 2\varepsilon_{13} \ 2\varepsilon_{12}] \quad (\text{A.2})$$

According to Eq. 8-10, the elastic parts of the Maxwell E_0 and Kelvin-Voigt E_1 elements (see Fig. 3 for a definition of the indices) are decomposed into shear J_0, J_1 and bulk B_0, B_1 components

$$J_i = \frac{2(1 + \nu)}{E_i} \quad (\text{A.3})$$

$$B_i = \frac{3(1 - 2\nu)}{E_i} \quad (\text{A.4})$$

with a constant (time independent) Poisson's ratio ν as discussed in Section 3.2.2. The time-dependent shear $J^*(t)$ and bulk $B^*(t)$ compliances correspond to the viscoelastic response of the Burgers model and are defined as

$$J^*(t) = \frac{1}{2} \left[J_0 + J_1 \left(1 + \frac{\tau(e^{-\Delta t/\tau} - 1)}{\Delta t} \right) \right] \quad (\text{A.5})$$

$$B^*(t) = \frac{1}{3} \left[B_0 + B_1 \left(1 + \frac{\tau(e^{-\Delta t/\tau} - 1)}{\Delta t} \right) \right] \quad (\text{A.6})$$

where $\tau = \eta_1/E_1$ denotes the relaxation time of the Kelvin-Voigt element. The constitutive equation to calculate the trial stress increment is then given by

$$\begin{aligned} \Delta \boldsymbol{\sigma}_{\text{tr}} = & \left[\frac{1}{J^*} \mathbf{M}_{\text{d}}^* + \frac{1}{B^*} \mathbf{M}_{\text{b}} \right] \Delta \boldsymbol{\varepsilon} - \frac{\Delta t}{\eta_0} \left[\frac{1}{J^*} \mathbf{M}_{\text{d}}^{**} + \frac{1}{B^*} \mathbf{M}_{\text{b}} \right] \boldsymbol{\sigma}(t) \\ & - (e^{-\Delta t/\tau} - 1) \left[\frac{1}{J^*} \mathbf{M}_{\text{d}}^{***} \boldsymbol{\varepsilon}_{\text{d}}^{\text{inh}}(t - \Delta t) + \frac{1}{B^*} \mathbf{M}_{\text{b}} \boldsymbol{\varepsilon}_{\text{b}}^{\text{inh}}(t - \Delta t) \right] \end{aligned} \quad (\text{A.7})$$

where the second term $\Delta t/\eta_0[\dots]\boldsymbol{\sigma}(t)$ represents the viscous response due to the free dashpot of the Maxwell model and the strain components $\boldsymbol{\varepsilon}^{\text{inh}}(t-\Delta t)$ refer to the inherited part from the previous time increment (Eq. A.15 and A.16).

The coupling matrix for the deviatoric components ($\mathbf{M}_{\text{d}}, \mathbf{M}_{\text{d}}^*, \mathbf{M}_{\text{d}}^{**}$ and $\mathbf{M}_{\text{d}}^{***}$) is defined as

$$\mathbf{M}_{\text{d}} = \begin{bmatrix} 2/3 & -1/3 & -1/3 & 0 & 0 & 0 \\ -1/3 & 2/3 & -1/3 & 0 & 0 & 0 \\ -1/3 & -1/3 & 2/3 & 0 & 0 & 0 \\ & 0 & 0 & 0 & a & 0 \\ & 0 & 0 & 0 & 0 & a \\ & 0 & 0 & 0 & 0 & 0 \end{bmatrix} \quad (\text{A.8})$$

with $a=2$ for \mathbf{M}_d , $a=1$ for \mathbf{M}_d^* , $a=3/2$ for \mathbf{M}_d^{**} and $a=1/2$ for \mathbf{M}_d^{***} . For the bulk components, it takes the form of

$$\mathbf{M}_b = \begin{bmatrix} 1/3 & 1/3 & 1/3 & 0 & 0 & 0 \\ 1/3 & 1/3 & 1/3 & 0 & 0 & 0 \\ 1/3 & 1/3 & 1/3 & 0 & 0 & 0 \\ 0 & 0 & 0 & 0 & 0 & 0 \\ 0 & 0 & 0 & 0 & 0 & 0 \\ 0 & 0 & 0 & 0 & 0 & 0 \end{bmatrix} \quad (\text{A.9})$$

For each call of the material subroutine, the trial stress increment is initially calculated under application of the stress dependent model parameters E_1 , η_0 , η_1 from the last time increment (an arbitrary value within the range specified in Fig. 6 can be chosen for the first time increment of the simulation step). The trial stress increment is then added to the old value of stress $\boldsymbol{\sigma}(t)=\boldsymbol{\sigma}(t-\Delta t)+\Delta\boldsymbol{\sigma}_{tr}$ and the equivalent stress for $\boldsymbol{\sigma}(t)$ is formed according to Eq. 14.

Based on the equivalent stress σ_{eq} , the model parameters E_1 , η_0 , η_1 are updated by Eq. 11-13 and the values of $J^*(t)$ and $B^*(t)$ are recalculated by Eq. A.5 and A.6. To apply the Newton procedure and to calculate a residual as specified in Fig. 4, the trial stress increment $\Delta\boldsymbol{\sigma}_{tr}$ needs to be converted into a trial strain increment $\Delta\boldsymbol{\varepsilon}_{tr}$ using the updated values of $J^*(t)$ and $B^*(t)$

$$\Delta\boldsymbol{\varepsilon}_{tr} = [J^*\mathbf{M}_d + B^*\mathbf{M}_b]\Delta\boldsymbol{\sigma}_{tr} + \frac{\Delta t}{\eta_0}\mathbf{M}_x\boldsymbol{\sigma}(t) \quad (\text{A.10})$$

$$+ (e^{-\Delta t/\tau} - 1)[\mathbf{M}_d\boldsymbol{\varepsilon}_d^{\text{inh}}(t - \Delta t) + \mathbf{M}_b\boldsymbol{\varepsilon}_b^{\text{inh}}(t - \Delta t)]$$

where \mathbf{M}_d and \mathbf{M}_b are specified by Eq. A.8 and A.9 and

$$\mathbf{M}_x = \begin{bmatrix} 1 & 0 & 0 & 0 & 0 & 0 \\ 0 & 1 & 0 & 0 & 0 & 0 \\ 0 & 0 & 1 & 0 & 0 & 0 \\ 0 & 0 & 0 & 3 & 0 & 0 \\ 0 & 0 & 0 & 0 & 3 & 0 \\ 0 & 0 & 0 & 0 & 0 & 3 \end{bmatrix} \quad (\text{A.11})$$

A residual strain $\Delta\boldsymbol{\varepsilon}_{res}=\Delta\boldsymbol{\varepsilon}_{tr}-\Delta\boldsymbol{\varepsilon}$ is formed by subtraction of the strain increment given by the FE software $\Delta\boldsymbol{\varepsilon}$ from the trial strain increment. A convergence criterium is defined as

$$\frac{\|\Delta\boldsymbol{\varepsilon}_{\text{res}}\|}{\|\Delta\boldsymbol{\varepsilon}\|} \leq 10^{-6} = c_{\text{tol}} \quad (\text{A.12})$$

where $\|\cdot\|$ denotes the Euclidean norm. A maximum of $n_{\text{max}}=15$ Newton iterations is performed to compute the updated trial stress increment $\Delta\boldsymbol{\sigma}_{\text{tr}}^{n+1}$ (otherwise, the procedure is aborted)

$$\Delta\boldsymbol{\sigma}_{\text{tr}}^{n+1} = \Delta\boldsymbol{\sigma}_{\text{tr}}^n - \left(\frac{1}{J^*} \mathbf{M}_{\text{d}}^{***} + \frac{1}{B^*} \mathbf{M}_{\text{b}} \right) \Delta\boldsymbol{\varepsilon}_{\text{res}} \quad (\text{A.13})$$

At the end of the material subroutine, the stress increment which is returned to the FE solver is updated with the latest value of the trial stress increment

$$\Delta\boldsymbol{\sigma} = \Delta\boldsymbol{\sigma}_{\text{tr}}^n \quad (\text{A.14})$$

The strain components of the Kelvin-Voigt element need to be saved in state variables. For this purpose, they are updated according to

$$\boldsymbol{\varepsilon}_{\text{d}}^{\text{inh}}(t) = e^{-\Delta t/\tau} \boldsymbol{\varepsilon}_{\text{d}}^{\text{inh}}(t - \Delta t) + \frac{J_1 \tau}{2\Delta t} (1 - e^{-\Delta t/\tau}) \mathbf{M}_{\text{d}} \Delta\boldsymbol{\sigma} \quad (\text{A.15})$$

$$\boldsymbol{\varepsilon}_{\text{b}}^{\text{inh}}(t) = e^{-\Delta t/\tau} \boldsymbol{\varepsilon}_{\text{b}}^{\text{inh}}(t - \Delta t) + \frac{B_1 \tau}{3\Delta t} (1 - e^{-\Delta t/\tau}) \mathbf{M}_{\text{b}} \Delta\boldsymbol{\sigma} \quad (\text{A.16})$$

The current values of the model parameters E_1 , η_0 , η_1 are saved in additional state variables.

Finally, the tangential matrix is updated with

$$\frac{d\Delta\boldsymbol{\sigma}}{d\Delta\boldsymbol{\varepsilon}} = \frac{1}{J^*} \mathbf{M}_{\text{d}}^{***} + \frac{1}{B^*} \mathbf{M}_{\text{b}} \quad (\text{A.17})$$

8. References

- [1] Thomason JL, Vlug MA, Schipper G Krikor HGLT. Influence of fibre length and concentration on the properties of glass fibre-reinforced polypropylene: Part 3. Strength and strain at failure. Composites Part A 27A (1996) 1075-1084.
- [2] Leaderman, H. Elastic and Creep Properties of Filamentous Materials and Other High Polymers. Textile Foundation, Washington, DC, 1943.
- [3] Schapery, RA. On the Characterization of Nonlinear Viscoelastic Materials.

Polymer Engineering and Science 9 (1969) 295-310.

[4] Findley WN, Lai JS, Onaran K. Creep and Relaxation of Nonlinear Viscoelastic Materials. New York: Dover Publications.

[5] Lai J, Bakker A. 3-D schapery representation for non-linear viscoelasticity and finite element implementation. Computational Mechanics 18 (1996) 182-191.

[6] Haj-Ali RM, Muliana AH. Numerical finite element formulation of the Schapery non-linear viscoelastic material model. International Journal for Numerical Methods in Engineering 59 (2004) 25-45.

[7] Woldekidan MF. Response Modelling of Bitumen, Bituminous Mastic and Mortar. PhD thesis, Delft University of Technology, 2011.

[8] Scott DW, Lai JS, Zureick AH. Creep behavior of Fiber-Reinforced Polymeric composites: A Review of the Technical Literature. Journal of Reinforced Plastics and Composites 14 (1995) 588-617.

[9] Lou YC, Schapery RA. Viscoelastic Characterization of a Nonlinear Fiber-Reinforced Plastic. J. Composite Materials 5 (1971) 208-234.

[10] Greco A, Musardo C, Maffezzoli A. Flexural creep behavior of PP matrix woven composite. Composites Science and Technology 67 (2007) 1148-1158.

[11] Houshyar S, Shanks RA, Hodzic A. Tensile creep behavior of polypropylene fibre reinforced polypropylene composites. Polymer Testing 24 (2005) 257-264.

[12] Howard CM, Hollaway L. The characterization of the non-linear viscoelastic properties of a randomly orientated fibre/matrix composite. Composites 18-4 (1987) 317-323.

[13] Mori T, Tanaka K. Average stress in matrix and average elastic energy of materials with misfitting inclusions. Acta Metallurgica 21 (1973) 571-574.

[14] Nguyen BN et al. Fiber length and Orientation in Long-Fiber Injection-Molded Thermoplastics - Part I: Modeling of Microstructure and Elastic Properties. Journal of Composite Materials 42 (2008) 1003-1029.

- [15] Garesci F, Fliegner S. Young's modulus prediction of long fiber reinforced thermoplastics. *Composites Science and Technology* 85 (2013) 142-147.
- [16] Buck F et al. Two-scale structural mechanical modeling of long fiber reinforced thermoplastics. *Composites Science and Technology* 117 (2015) 159-167.
- [17] Brinson LC, Lin WS. Comparison of micromechanics methods for effective properties of multiphase viscoelastic composites. *Composite Structures* 41 (1998) 353-367.
- [18] Brinson LC, Knauss WG. Finite Element Analysis of Multiphase Viscoelastic Solids. *J. Appl. Mech.* 59 (1992) 730-737.
- [19] Matzenmiller A, Gerlach S. Micromechanical modeling of viscoelastic composites with compliant fiber-matrix bonding. *Computational Materials Science* 29 (2004) 283-300.
- [20] Fisher FT, Brinson LC. Viscoelastic interphases in polymer-matrix composites: theoretical models and finite-element analysis. *Composites Science and Technology* 61 (2001) 731-748.
- [21] Haj-Ali RM, Muliana AH. A multi-scale constitutive formulation for the nonlinear viscoelastic analysis of laminated composite materials and structures. *International Journal of Solids and Structures* 41 (2004) 3461-3490.
- [22] Fliegner S, Luke M, Gumbsch P. 3D microstructure modeling of long fiber reinforced thermoplastics. *Composites Science and Technology* 104 (2014) 136-145.
- [23] Fliegner S, Micromechanical finite element modeling of long fiber reinforced thermoplastics, PhD thesis, Karlsruhe Institute of Technology (KIT), 2015, DOI: 10.5445/IR/1000051015
- [24] Henning F, Ernst H, Brüssel R, Geiger O, Krause W. LFTs for automotive applications. *Reinforced Plastics* 49 (2005) 24-33.
- [25] Kabel M, Fliegner S, Schneider M. Mixed boundary conditions for FFT-based homogenization at finite strains. *Comput Mech* 57 (2016) 193-210.
- [26] Tinevez JY. Directionality plugin for ImageJ. <http://fiji.sc/wiki/index.php/Directionality>.

[27] Brinson HF, Brinson LC. Polymer Engineering Science and Viscoelasticity - An Introduction. Springer (2008) pp 356.

[28] Taylor RL, Pister KS, Goudreau, GL. Thermomechanical analysis of viscoelastic solids. International Journal for numerical methods in engineering 2 (1970) 45-59.

[29] Brinson LC, Knauss WG. Thermorheologically complex behavior of multi-phase viscoelastic materials. J. Mech. Phys. Solids 39 (1991) 859-880.

9. Figures and Tables

Figure 1: Close-up of the finite element mesh of a PPGF30 (13.2 vol-%) LFT structure. Full details on the applied microstructure generation procedure are described in [22,23].

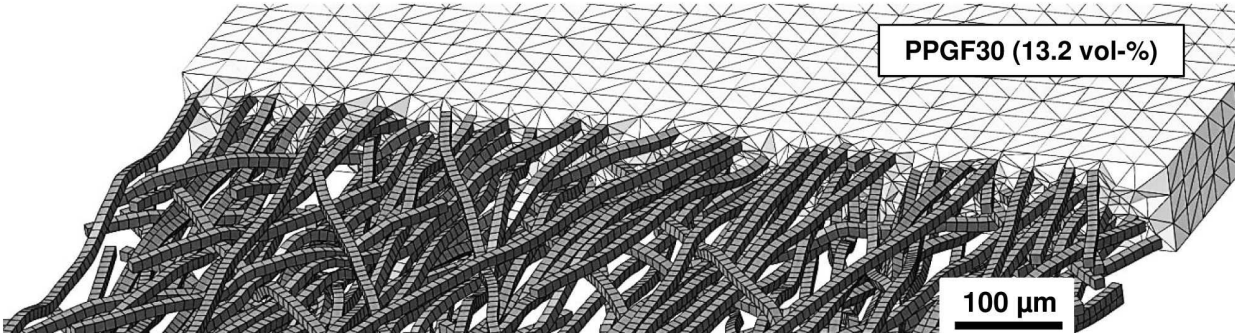


Figure 2: A small section of a computer generated fiber structure (left, top) of PPGF30 compared to a CT scan (left, bottom) and probability density functions of the planar fiber orientation distributions of the computer generated structure compared to the CT scan (right).

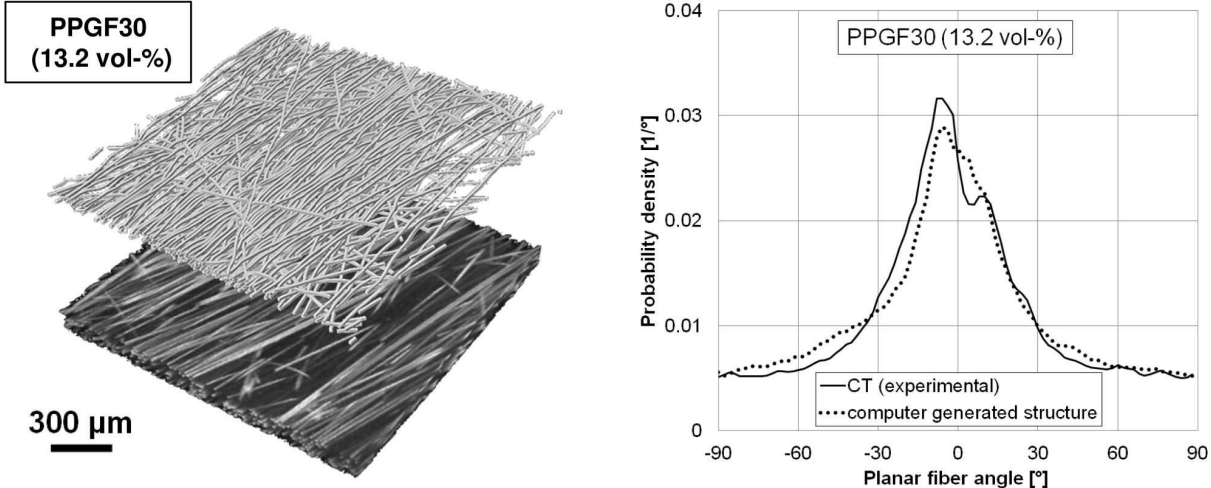


Figure 3: Rheological notation of the viscoelastic Burgers model.

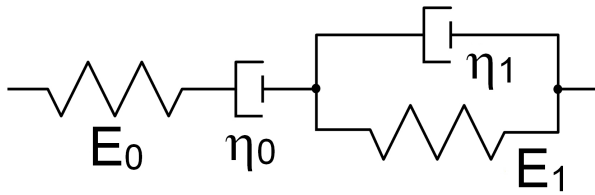


Figure 4: Flowchart of the nonlinear viscoelastic Burgers model as implemented by a user material subroutine.

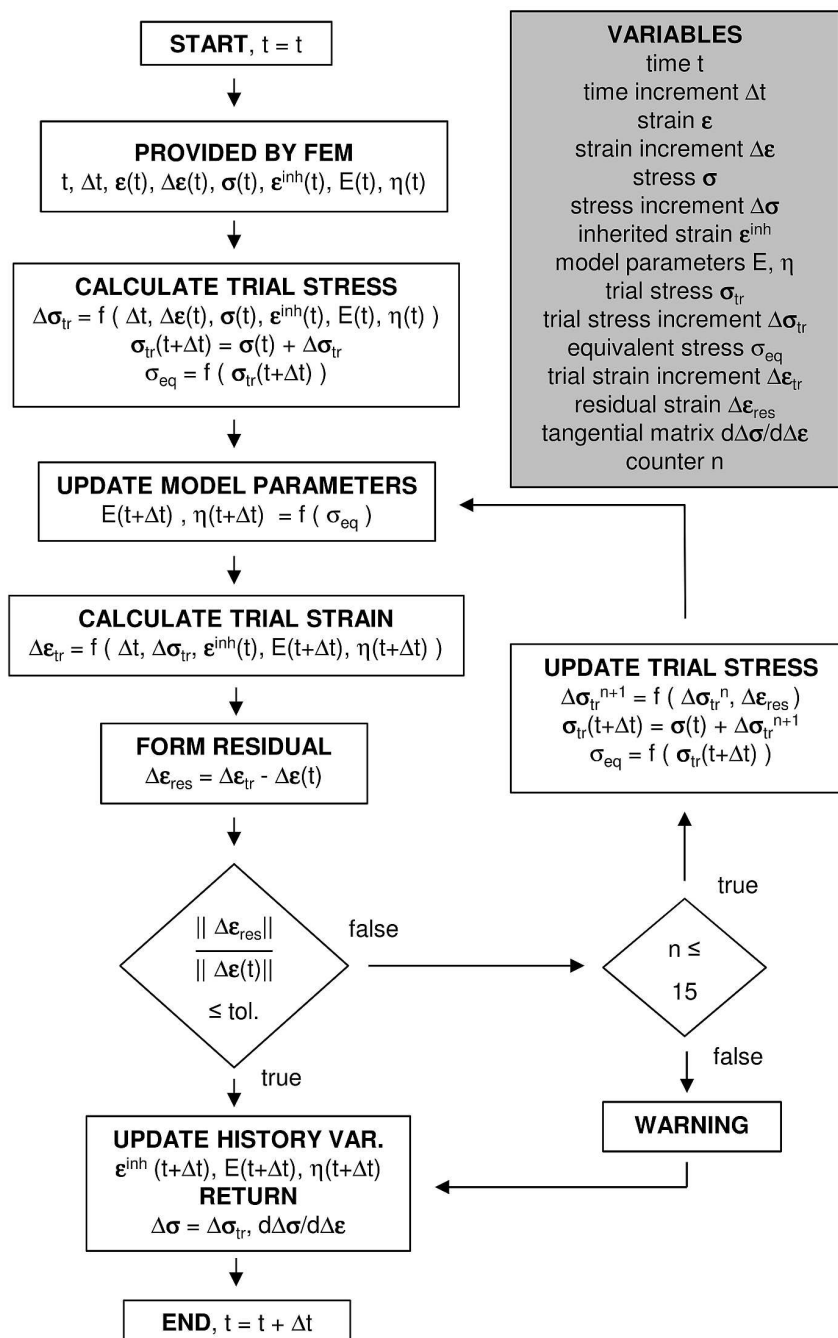


Figure 5: Creep-recovery experiments on matrix substance specimens under varying stress levels from 2.5 to 12.5 MPa to calibrate the nonlinear viscoelastic Burgers model.

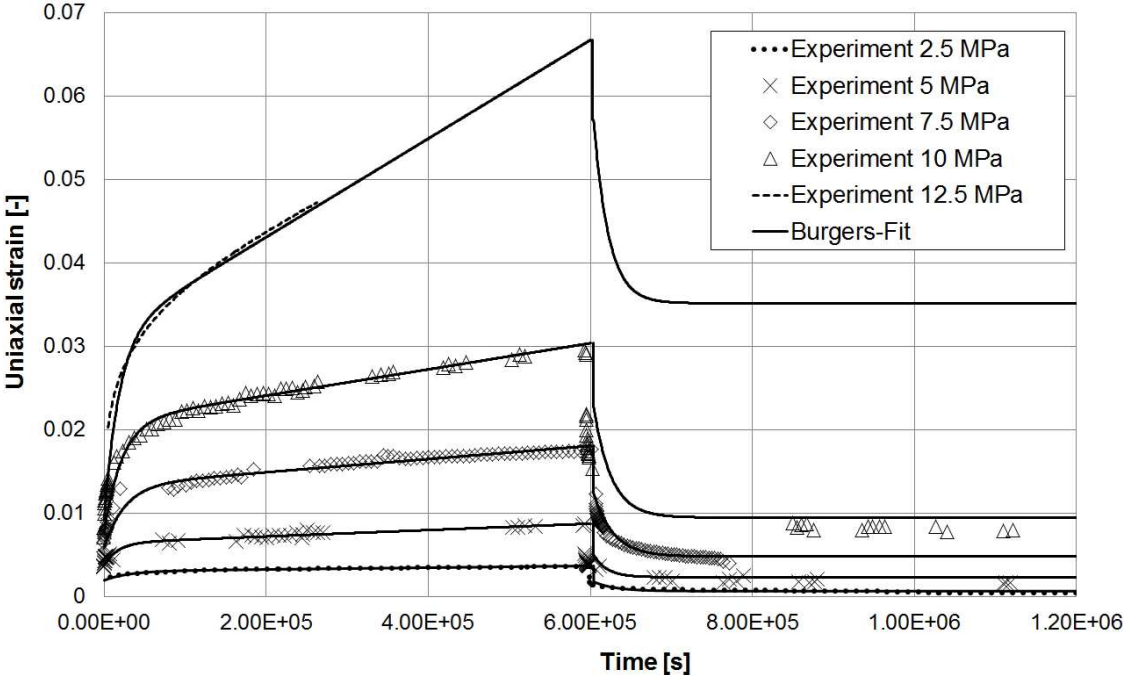


Figure 6: Stress-dependent Burgers parameters E_1 , η_0 and η_1 and fit functions (Eq. 11 - 13).

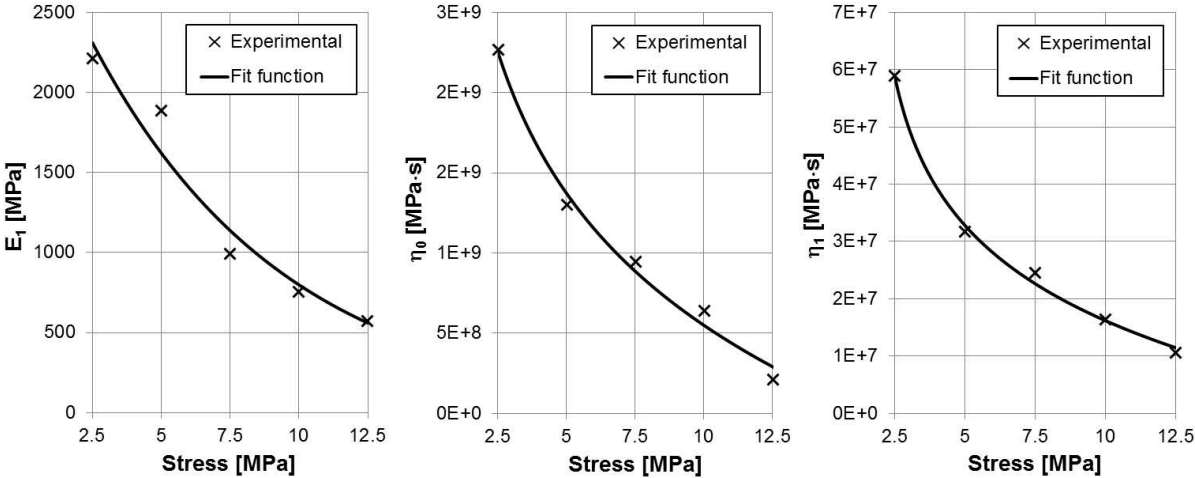


Figure 7: Creep curves of PPGF10 (3.8 vol-%) under varying stress levels and two different orientations (0 and 90° relative to flow direction).

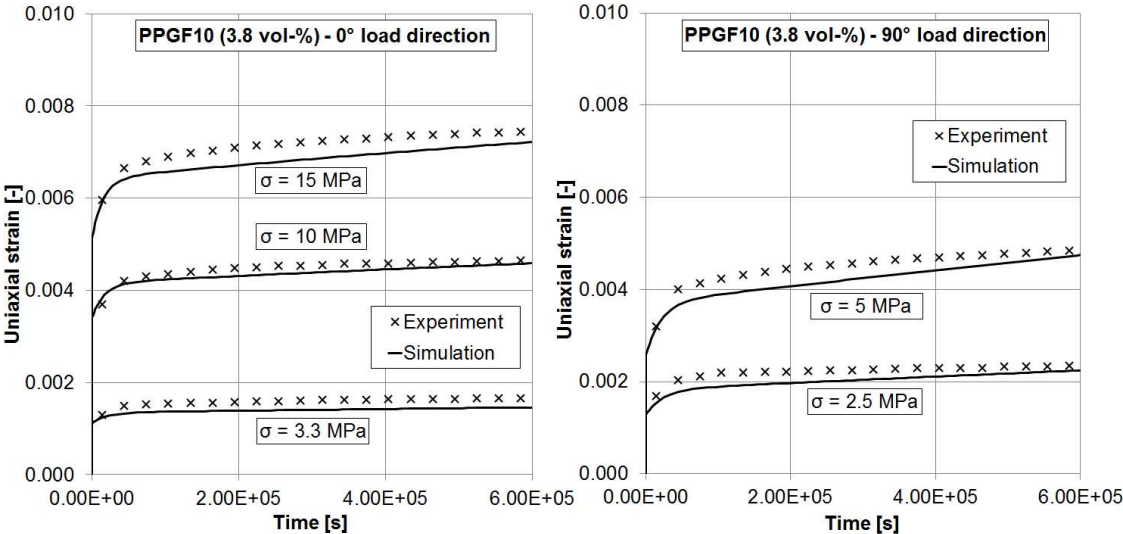


Figure 8: Creep curves of PPGF20 (8.1 vol-%) under varying stress levels and two different orientations (0 and 90° relative to flow direction).

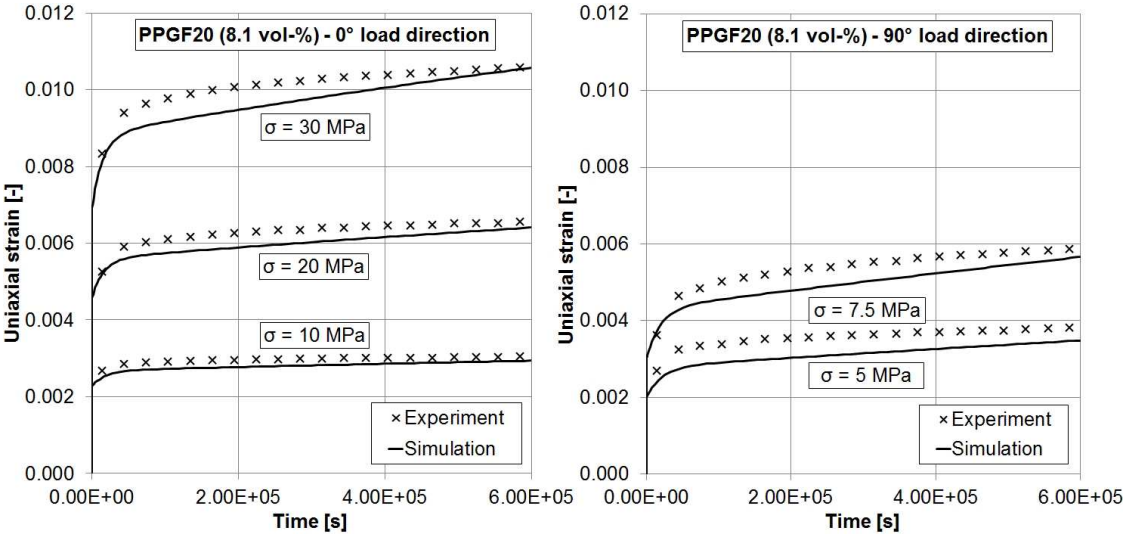


Figure 9: Creep curves of PPGF30 (13.2 vol-%) under varying stress levels and two different orientations (0 and 90° relative to flow direction).

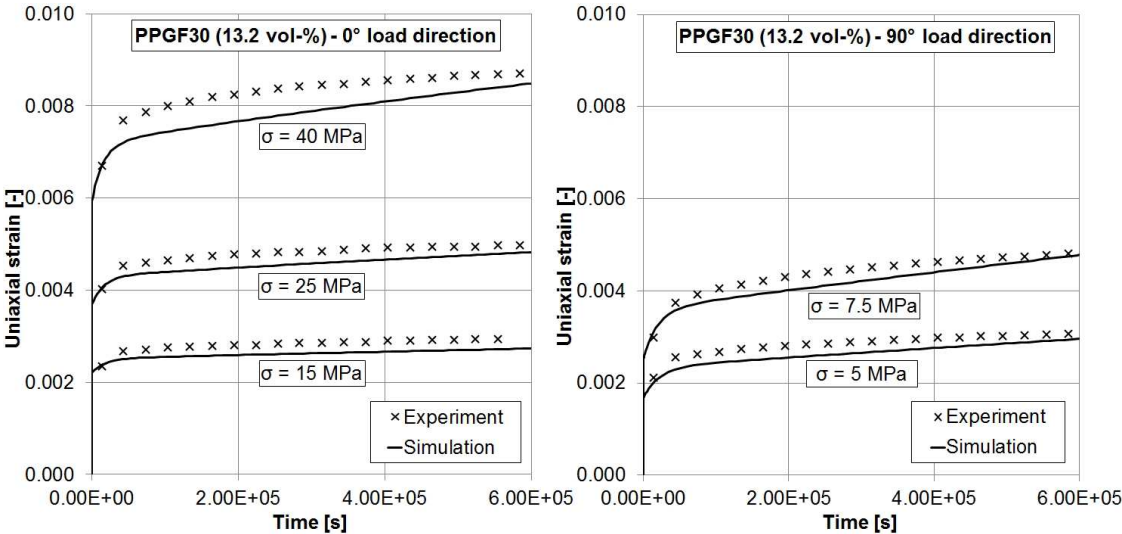


Figure 10: The effects of nonlinearity demonstrated for PPGF30 (13.2 vol-%), 0° load direction and a stress level of 40 MPa by comparison of the resulting creep curves for different variants of the matrix model. The nonlinear model (stress-dependent parameters, Eq. 11-13) is compared to two boundary curves of the linear model (constant parameters, lower boundary: $E_1=2310$ MPa, $\eta_0=2.26 \cdot 10^9$ MPa·s, $\eta_1=5.88 \cdot 10^7$ MPa·s corresponding to an indicator stress of 2.5 MPa / upper boundary: $E_1=560$ MPa, $\eta_0=2.93 \cdot 10^8$ MPa·s, $\eta_1=1.15 \cdot 10^7$ MPa·s corresponding to an indicator stress of 12.5 MPa, see Fig. 6).

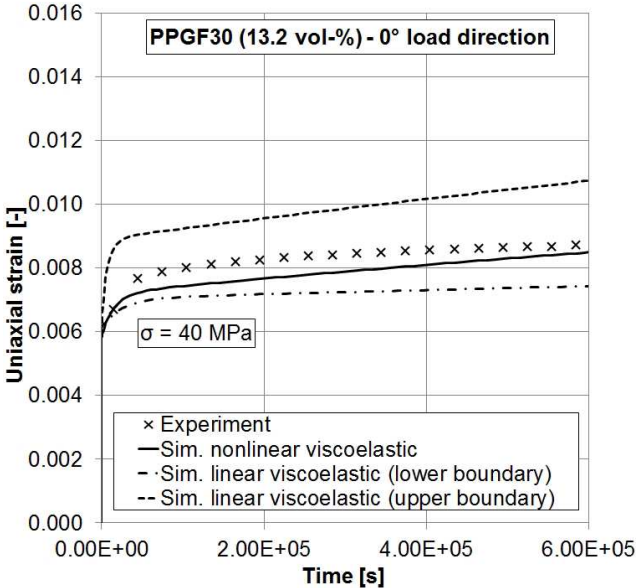


Figure 11: Evolution of the von Mises stress (Eq. 14, top), the equivalent deviatoric strain (Eq. 15, middle) and the hydrostatic strain (Eq. 16, bottom) within an exemplary section of the PPGF30 structure (cut through the model) under the highest investigated stress level of 40 MPa at $t = 600 \text{ s}$ (left) and $t = 6 \cdot 10^5 \text{ s}$ (right).

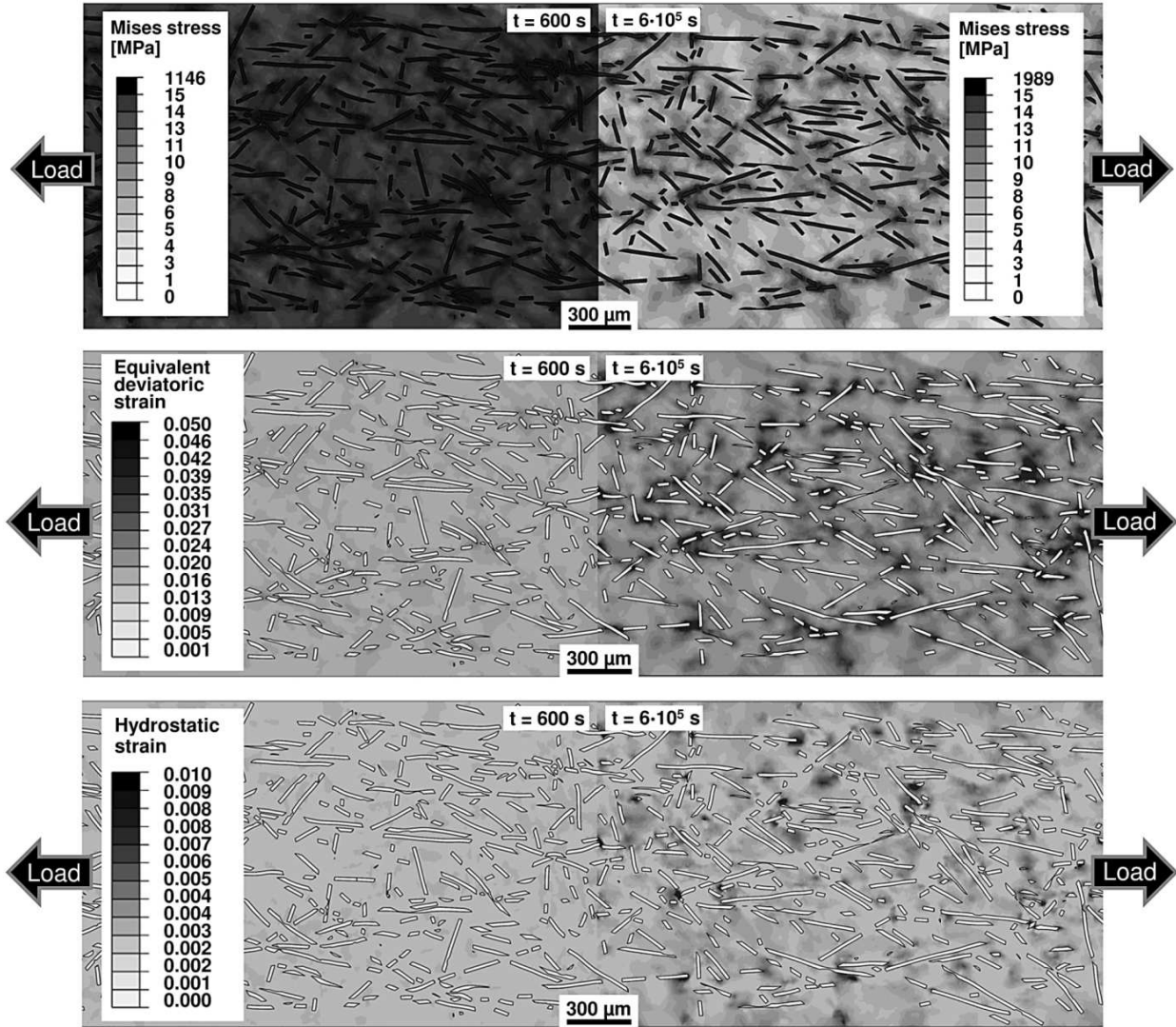


Table 1: Characteristic values of the investigated LFT structures. Details can be found in [22,23].

Material	Fiber vol. frac. [%]	Dimensions [mm ³]	Element count	Fiber count	Total fiber length [mm]	Mean weighted fiber length [mm]
PPGF10	3.82	50 x 2.75 x 0.125	$7.39 \cdot 10^6$	1633	3056	10.1
PPGF20	8.03	50 x 2.75 x 0.099	$8.73 \cdot 10^6$	2605	5048	9.4
PPGF30	13.15	50 x 1.5 x 0.134	$9.66 \cdot 10^6$	3256	6067	8.1

Table 2: Parameters of the nonlinear viscoelastic model of the polypropylene matrix and the linear elastic model of the glass fibers.

Parameter	Value	Unit	Description
E_0	1250	MPa	Instantaneous elastic stiffness (elastic branch of the Maxwell element)
E_1	560 - 2310 (stress dependent)	MPa	Elastic branch of the Kelvin-Voigt element, stress dependency described by Eq.11
η_0	$2.93 \cdot 10^8$ - $2.26 \cdot 10^9$ (stress dependent)	MPa·s	Viscous branch of the Maxwell element, stress dependency described by Eq. 12
η_1	$1.15 \cdot 10^7$ - $5.88 \cdot 10^7$ (stress dependent)	MPa·s	Viscous branch of the Kelvin-Voigt element, stress dependency described by Eq. 13
ν	0.35	-	Poisson's ratio of the matrix
n_{\max}	15	-	Maximum number of Newton iterations (Eq. A.13)
c_{tol}	10^{-6}	-	Tolerance / convergence criterion (Eq. A.12)
E_f	$7.2 \cdot 10^4$	MPa	Elastic modulus of the fibers
ν_f	0.22	-	Poisson's ratio of the fibers